EUROPEAN JOURNAL OF COMPUTATIONAL MECHANICS, 2017
VOL. 26, NOS. 5–6, 557–583
https://doi.org/10.1080/17797179.2017.1386022

Taylor & Francis
Taylor & Francis Group

Application of the adjoint optimisation of shock control bump for ONERA-M6 wing

A. Nejati[a] and K. Mazaheri[b]

[a]Aerospace Engineering, Science and Research Branch of Islamic Azad University, Tehran, Iran; [b]Aerospace Engineering, Sharif University of Technology, Tehran, Iran

ABSTRACT

This article is devoted to the numerical investigation of the shock wave/boundary layer interaction (SWBLI) as the main factor influencing the aerodynamic performance of transonic bumped airfoils and wings. The numerical analysis is conducted for the ONERA-M6 wing through a shock control bump (SCB) shape optimisation process using the adjoint optimisation method. SWBLI is analyzed for both clean and bumped airfoils and wings, and it is shown how the modified wave structure originating from upstream of the SCB reduces the wave drag, by improving the boundary layer velocity profile downstream of the shock wave. The numerical simulation of the turbulent viscous flow and a gradient-based adjoint algorithm are used to find the optimum location and shape of the SCB for the ONERA-M6 airfoil and wing. Two different geometrical models are introduced for the 3D SCB, one with linear variations, and another with periodic variations. Both configurations result in drag reduction and improvement in the aerodynamic efficiency, but the periodic model is more effective. Although the three-dimensional flow structure involves much more complexities, the overall results are shown to be similar to the two-dimensional case.

ARTICLE HISTORY
Received 23 April 2017
Accepted 24 September 2017

KEYWORDS
Transonic wing; drag reduction; shock control bump; adjoint optimisation method; three-dimensional bump

1. Introduction

Reducing aerodynamic drag in the transonic regime is one of the main challenges facing airplane design engineers. Simultaneous presence of several physical phenomena, i.e. shock waves, flow instability, shock wave/boundary layer interaction (SWBLI), boundary layer thickening and boundary layer separation (Abdellah, 2012; Abdul Hamid, Toufique Hasan, Alimuzzaman, Matsuo, & Setoguchi, 2014), increase the flow complexity in this regime. Due to these physical phenomena, there is a critical Mach number which is a function of the shape and flight conditions, above which the aerodynamic performance falls rapidly.

CONTACT A. Nejati a_nejati@srbiau.ac.ir

Adaptive wings may be employed to postpone this abrupt performance variation in a transonic flight. An elementary usage of this idea is done by Evans, Hynes, Norman, and Thomasson (1984). They incorporated leading and trailing edge variable camber mechanisms to improve the manoeuvrability and performance in F-111 airplane. In 1992, Ashill, Fulker, and Shires (1992) introduced the shock control bump (SCB) to be applied in natural laminar flow (NLF) airfoils, a new concept in adaptive surface design which uses only a confined region of the airfoil surface and has a significant effect on the strength of the incurring shock wave.

A bump is formed on the upper surface of the wing to produce isentropic compression waves upstream of the normal shock wave. While the flow passes through these isentropic compression waves, it experiences a gradual reduction in Mach number and also a gradual increase in the static pressure rather than an abrupt change associated with a strong normal shock wave. As the Mach number of the flow is decreased towards the crest of the bump, a weaker normal shock wave resulting in a lower wave drag will occur. The whole flow pattern is more stable than a clean airfoil due to improve in the pressure gradient, and results in a better pressure recovery and a reduced drag, a higher lift, and also delayed (Milholen & Lewis, 2005; Patzold, Lutz, Kramer, & Wagner, 2006).

Although traditional methods of flow control such as suction/blowing, vortex generators and cavity ventilation are studied extensively and are proved to be quite effective regarding aerodynamics performance in transonic regimes (Stanewsky, Delery, Fulker, & de Matteis, 2002), detailed studies on SCBs have shown more promising results, especially compared to cavity ventilation, suction (Qin, Zhu, & Shaw, 2004; Stanewsky et al., 2002) and thermal methods (Bhattacharjee, Ahsan, & Mohammad, 2007).

The efficacy of a SCB is quite sensitive to its shape and location, which of course depends strongly on the airfoil or wing geometry and also free stream conditions. Diverse studies are devoted to the design of the shape and location of the bump, e.g. (Patzold et al., 2006; Sommerer, Lutz, & Wagner, 2000; Tian, Liu, & Feng, 2011). These studies can be divided into two categories: (a) shape optimisation, e.g. (Patzold et al., 2006; Sommerer et al., 2000; Tian, Liu, & Li, 2014), and (b) parametric analysis, e.g. (Tian et al., 2011). All the above studies are devoted to 2D SCBs, while all real applications are three-dimensional. Although many other articles have studied 3D SCBs, most of them have only considered an infinite span wing, and they suffer from lack of a strong optimisation tool. Wong, Le Moigne, and Qin (2007) have optimised a bump on a 3D wing based on Euler Equations (i.e. an inviscid flow solver) and have not considered the viscous effects, which is necessary to study shock and boundary layer interactions. Furthermore, hybrid flow control methods based on SCBs are also used to take simultaneous advantage of both concepts. For instance, Yagiz, Kandil, and Pehlivanoglu (2012) have studied wave drag reduction based on bump and suction/injection in a transonic regime. Lee, Bugeda, Periaux, and Onete (2010, 2012) have also studied the SCB

shape design optimisation in flow fields with uncertainty in boundary-layer transition locations, using robust evolutionary algorithms.

Authors have recently used a single-point evolutionary optimisation scheme and also the multi-point adjoint gradient-based method to improve application of the SCB for better aerodynamic performance of two transonic airfoils, under a constant angle of attack condition (Mazaheri, Kiani, Nejati, Zeinalpour, & Taheri, 2015; Mazaheri, Nejati, Kiani, & Taheri, 2016). We have also studied the robust optimisation of 2D SCBs and the multi-point optimisation of a very simple 3D SCB (Mazaheri, Nejati, & Kiani, 2016). Moreover, we have achieved optimisation of the hybrid usage of suction with a SCB, and blowing with a SCB in a constant lift condition (Mazaheri & Nejati, 2016) and also optimisation of the simultaneous usage of all three flow control methods together (suction-SCB-blowing) (Nejati & Mazaheri, 2016).

Qin, Wong, and Le Moigne (2008) have used two-dimensional and three-dimensional bumps to optimise an un-swept NLF wing (an RAE-5243 airfoil) at transonic speeds to achieve wave drag reductions. They have investigated a segment of a 3D infinite NLF wing. Many features of a real wing are missing in their simulation. They only used six design parameters, and a low Mach number of 0.68. Their results show that, despite the significant difference in their geometrical shapes, the optimised three-dimensional bumps are as effective as the optimised two-dimensional bumps in terms of the total drag reduction at the given design point. Ogawa, Babinsky, Pätzold, and Lutz (2008) have performed an extensive experimental investigation and a computational study on a three-dimensional rounded bump in a channel flow for a series of span-wise rounded bumps mounted on a transonic airfoil, at $M = 0.76$. They also investigated only a segment of an infinite wing, and also did not use optimisation tools. In both cases, wave drag reduction and mild control effects of the boundary layer were observed.

Colliss, Babinsky, Nubler, and Lutz (2014) have presented a joint experimental and numerical approach to three-dimensional SCB research to bridge the gap between computational fluid dynamics and experiment. Bruce and Babinsky (2012) have carried out a fundamental experimental study on the flow structure around a single three-dimensional (3D) SCB mounted on a flat surface in a wind tunnel. Both groups, i.e. Colliss et al. (2014) and Bruce and Babinsky (2012), have analysed effects of a simple model 3D bump (a wedge bump) on an infinite wing, and have tried to understand the three-dimensional flow physics. They have not used any optimisation algorithm to optimise the SCB geometry. Eastwood and Jarrett (Eastwood & Jarrett, 2012) have done a computational study of the performance of three-dimensional bumps, relating the key bump design variables to the overall wing aerodynamic performance. They have also conducted a parametric optimisation of simple geometry SCBs, for an infinite wing at $M = 0.71$. Their geometrical model is a simple wedge shape, with two parameters. Since they have not used an optimisation tool, scope of their study is very limited.

Mayer, Lutz, and Kraemer (2015) have used an infinite wing and a wedge shaped SCB, with a limited optimisation tool. They have shown that shock control bumps (SCB) can additionally be used for buffet alleviation. Considering 3D SCBs as a novel sort of vortex generators, when carefully designed, these bumps introduce stream-wise vorticity into the flow and thereby prevent the boundary layer from early separation. They have also presented a strategy towards optimising SCBs for buffet alleviation. In their study, besides the theoretical idea of boundary layer enhancement by bump, a CFD-based process chain for bump optimisation has been presented. Koenig, Paetzold, Lutz, and Kraemer (2007) have studied the influence of trimming and aero-elasticity on the performance of an SCB. They have used a simple model for the SCB on a rigid wing with three design variables. Their results have shown that by using a SCB the wing performance improves about 2% which is much less than results presented here.

The main goal of this article is further extension of the SCB concept to improve the aerodynamic performance of real three-dimensional transonic wings. In this investigation, the root section of the ONERA-M6 wing which is a transonic airfoil is used for the optimisation of 2D SCBs. To investigate applicability of the SCB to finite three-dimensional wings, two different geometrical models, i.e. a SCB with linear variation and a SCB with periodic variation, are introduced for generation of 3D SCBs, and are implemented on an ONERA-M6 wing. An adjoint optimisation algorithm is used to find the optimum location and shape of the bumps. The flow structure around these bumps and their effects on the aerodynamic performance of the wing are analysed to have a better understanding of how this mechanism improves the aerodynamic performance of a wing in a transonic flow.

To simulate the flow dynamics, the RANS equations are applied. To calculate the convective fluxes in the numerical scheme, Roe approximations are used with the second order of accuracy (Blazek, 2005). The Menter form of the k-ω turbulence model is also used for the turbulence modelling (Wilcox, 2006). The steepest decent algorithm used in our optimisation scheme is based on references (Rao, 1996; Snyman, 2005). As it was mentioned above, in this article the adjoint optimisation algorithm is used to find the optimised geometry. In gradient-based schemes, the gradient of a cost function with respect to all design parameters is used to find the optimum configuration. While computation of the gradient evaluation is usually proportional to the number of design parameters, for a gradient-based adjoint method it is almost independent of the number of design parameters. Therefore, the total adjoint computational time is only a little more than the time devoted to the flow solver. In the CFD community, this was first observed in the initial research of Nadarajah and Jameson (Nadarajah & Jameson, 2000) regarding optimisation of transonic airfoils.

The study presented here is distinguished from the above studies by applying a stronger optimisation tool with much more design parameters (say, 35) to a real 3D finite wing at a very sensitive high Mach number. Other contributions of this work include introduction of two new 3D geometrical model for the SCB which

are very suitable for an automatic optimisation process. The main contributions of this article are as follows:

- Introducing and analysing the three- and the five-component wave structure over the transonic wings.
- Investigation on the boundary-layer pattern around the three-dimensional SCBs and their interaction with the shock wave.
- Introducing two new three-dimensional geometrical models for the 3D SCBs.
- Implementation and comparison of performance improvement for two different 3D SCBs optimised on an ONERA-M6 wing for transonic flow.

2. Problem definitions

Our target here is to use a single-point optimisation process to design an SCB which minimises an ONERA-M6 wing's drag coefficient for a selected flight condition. The geometrical data for the ONERA-M6 wing are given in Table 1. In this single-point optimisation, only one flight condition (given in Table 2) and a constant lift constraint is considered. We will first use the root section of the ONERA-M6 wing as a transonic airfoil, to find an optimised SCB and to investigate its effects in improvement in aerodynamic performance and in the flow structure. Then we will extend the idea to a 3D wing, and introduce two different three-dimensional geometrical models to generate SCBs for the wing, The shape and location of the SCBs are optimised for the same flight condition (given in Table 2) as the 2D case, and two- and three-dimensional results are compared with each other.

3. The flow governing equations and validation of the flow solver

The integral form of the Navier Stokes equations for each computational cell is introduced in Equation (1). In this equation $\mathbf{U}$, $\mathbf{f}_c$, $\mathbf{f}_v$ stand for the conservative variable vectors, the convection flux vector, and the viscous flux vector, respectively.

Table 1. The ONERA-M6 wing geometrical data.

Trailing-edge sweep	Leading-edge sweep	Taper ratio	Aspect ratio	Mean aerodynamic chord, c	Span, b
15.8°	30.0°	0.562	3.8	0.636	1.196

Table 2. Flight conditions for ONERA-M6 wing aerodynamic analysis.

Flow condition	Angle-of-sideslip (β)	Angle-of-attack (α)	Re_∞	M_∞
1	0.0	3.06	11.7×10^6	0.839

$$\frac{\partial}{\partial t}\int_{\Omega}\vec{\mathbf{U}}\,d\Omega+\oint_{\partial\Omega}\left(\vec{\mathbf{f}}_c-\vec{\mathbf{f}}_v\right)ds=0 \tag{1}$$

The finite-volume method is used for the flow field discretisation. The flux across each cell face is approximated using the Roe flux difference splitting method. For more details about the Roe averaged variables and discretisation procedure please see references (Blazek, 2005; Mazaheri, Nejati, Kiani, & Taheri, 2016).

The experimental results from Schmitt and Charpin (1979) have been used for the flow solver validation. A 3D finite-volume Navier–stokes RANS solver which is developed at CEAS (Centre of Excellence in Aerospace Systems) is used as the flow solver (Ramezani & Mazaheri, 2009). To validate the flow solver for a three-dimensional case, we have solved the flow around the ONERA-M6 wing for the flight condition given in Table 2. A structured algebraic grid shown in Figure 1 is used. The flow field is extended about 20 times the wing span in the span-wise, and the grid includes about 3.6 million cells (142 nodes around the airfoil, 150 for the rest, 100 nodes span-wise over the wing and 70 nodes normal to the airfoil). The symmetry plane $z/b = 0$ and the wing surface grid are also shown in Figure 1. The grid resolution is increased near the wing tip, which is rounded, to better resolve small flow structures in this region (see Figure 2). A 6×4.2 GHz CPU is used for this computation.

Figure 3 compares the pressure coefficient distribution in four different sections of the wing with experimental results presented in Schmitt and Charpin (1979). The numerical results follow the experimental results with an acceptable accuracy.

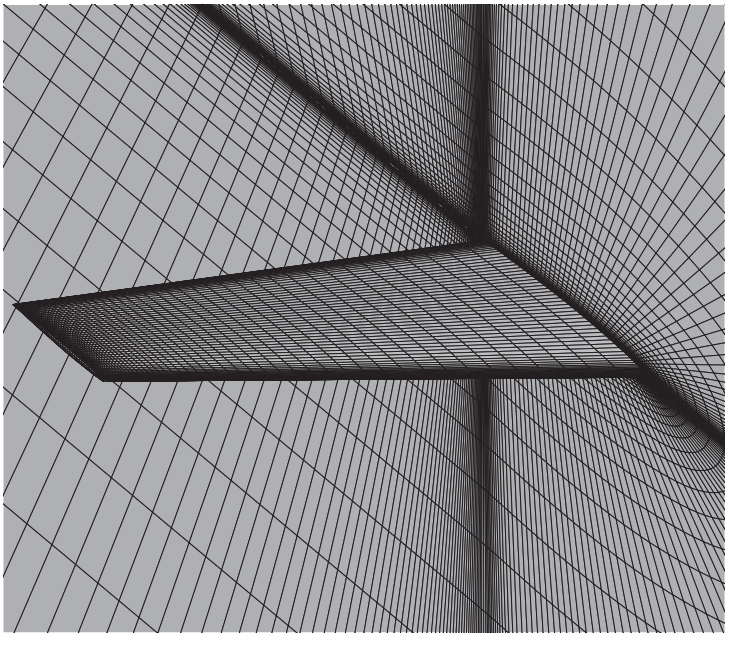

Figure 1. Sample grid generated around the ONERA-M6 wing.

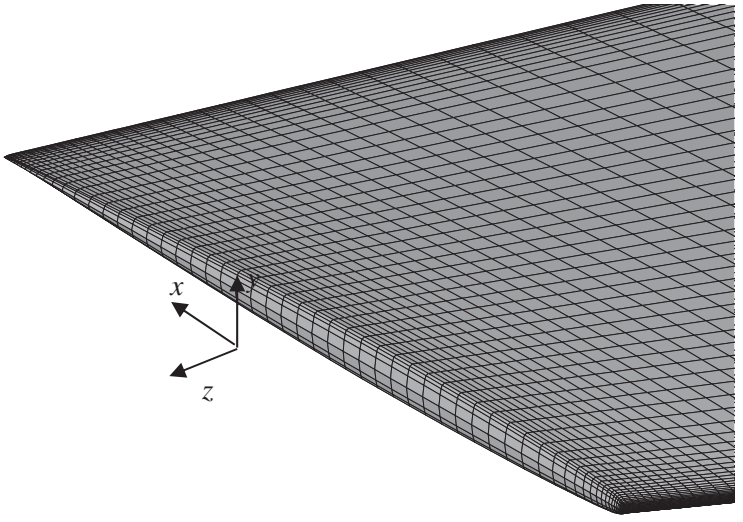

Figure 2. Grid quality around the ONERA-M6 tip.

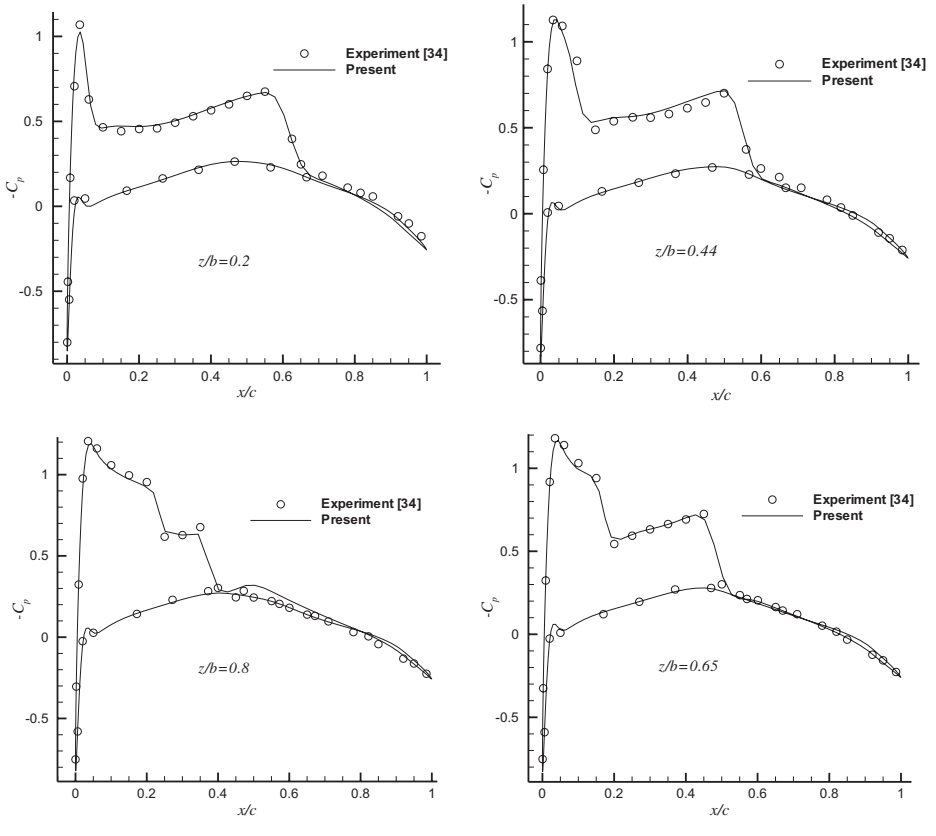

Figure 3. Comparison of the pressure coefficient distribution for flow around ONERA-M6 wing in four different stations.

The three-dimensional shock structure over the wing is resolved, and one observes that the shock location moves span-wise towards the leading edge because of the swept back configuration of the wing.

4. The optimisation algorithm and the adjoint method

In this research a gradient-based steepest descent algorithm is used to find the optimum point, by moving from the initial guess in the opposite direction of the gradient vector. In steepest descent algorithm, the design variables are updated as follows:

$$\mathbf{b}_{i+1} = \mathbf{b}_i + \lambda_i^* \mathbf{S}_i = \mathbf{b}_i - \lambda_i^* \nabla F_i \tag{2}$$

Details for the scheme and how to select the step size are given in (Mazaheri, Nejati, & Kiani, 2016). In this article, for computing the gradient of a cost function with respect to all design variables, we have used the adjoint method. For obtaining the adjoint equations, one may derive the governing equations for the viscous flow (i.e. 2D N-S equations) as:

$$\frac{\partial \mathbf{U}}{\partial t} + \frac{\partial \mathbf{f}_k^{inv}}{\partial x_k} - \frac{\partial \mathbf{f}_k^{vis}}{\partial x_k} = 0 \tag{3}$$

where $\mathbf{f}_{inv}$ and $\mathbf{f}_{vis}$ denote the inviscid and the viscous flux vectors. $\mathbf{U}$ is the vector of flow variables. Here the standard index notation was used. k in the above equation is the dummy index. Using a mathematical procedure explained in (Mazaheri, Nejati, Kiani, & Taheri, 2016; Nadarajah & Jameson, 2000) the viscous adjoint equation is derived as:

$$\frac{\partial \boldsymbol{\psi}}{\partial t} - \mathbf{A}_k^T \frac{\partial \boldsymbol{\psi}}{\partial x_k} - \mathbf{M}^{-T}\mathbf{K} = 0 \tag{4}$$

where,

$$\begin{aligned}
K_1 &= -\frac{p}{\rho^2}\frac{\partial}{\partial x_k}\left(\kappa \frac{\partial \psi_\Lambda}{\partial x_k}\right) \\
K_{k+1} &= \frac{\partial}{\partial x_m}\left[\mu\left(\frac{\partial \psi_{m+1}}{\partial x_k} + \frac{\partial \psi_{k+1}}{\partial x_m}\right) + \lambda \delta_{km}\frac{\partial \psi_{l+1}}{\partial x_l}\right] \\
&\quad + \frac{\partial}{\partial x_m}\left[\mu\left(u_m \frac{\partial \psi_\Lambda}{\partial x_k} + u_k \frac{\partial \psi_\Lambda}{\partial x_m}\right) + \lambda \delta_{km} u_l \frac{\partial \psi_\Lambda}{\partial x_l}\right] \\
&\quad -\tau_{km}\frac{\partial \psi_\Lambda}{\partial x_m} \qquad for \quad k = 1, 2 \\
K_4 &= \frac{1}{\rho}\frac{\partial}{\partial x_k}\left(\kappa \frac{\partial \psi_\Lambda}{\partial x_k}\right).
\end{aligned} \tag{5}$$

In Equation (4), $\mathbf{M}^{-T}$ is a transition matrix of non-conservative variables to conservative ones. Also, matrix $\mathbf{A}_k^T$ is defined by:

$$\mathbf{A}_k^T = \left(\frac{\partial \mathbf{f}_k^{inv}}{\partial \mathbf{U}} \right)^T \tag{6}$$

and the adjoint boundary condition for inverse design problems is:

$$\psi_{k+1} = -(p - p_{tar}) n_k \tag{7}$$

n_k is the surface normal vector. More details of the scheme and boundary conditions are given in (Mazaheri, Nejati, Kiani, & Taheri, 2016). Validation of this algorithm is straight forward (Mazaheri, Nejati, & Kiani, 2016; Mazaheri, Nejati, Kiani, & Taheri, 2016), and is not repeated here.

If the pressure and viscous drag coefficients are part of the cost function (instead of inverse design problems), a few modifications in the boundary conditions is required, which are described in details in Mazaheri, Nejati, and Kiani (2016) and Mazaheri, Nejati, Kiani, and Taheri (2016). To discretise the inviscid terms in the adjoint equation, a first order upwind scheme similar to the Roe's FDS method is used here. To compute the adjoint derivatives a second order central difference scheme is used (Details may be found in Anderson & Venkatakrishnan, 1997; Giles & Pierce, 1997).

5. Modelling of the 2D bump geometry

In this research, to model the 2D bump geometry the sine-function in Tian et al. (2011) is used with minor improvements. The Hicks-Henne formula (Equation (8)) is a sine-function that is able to create bumps with different heights, slopes, asymmetries and lengths. In Equation (8), h_B is the maximum bump height, t represents the slope parameter and x represents the length parameters which are non-dimensionalised with the bump length (l_B). All the geometrical details are shown in Figure 4.

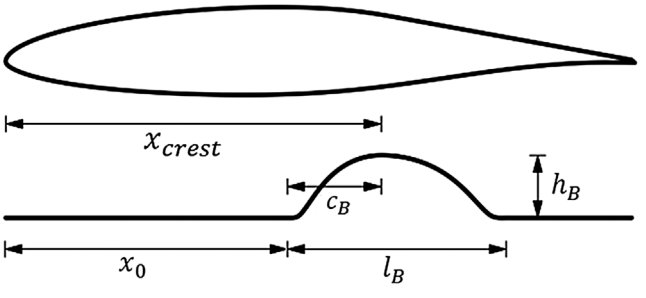

Figure 4. Parameters for designing a 2D bump.

$$f(x) = h_B\left(\sin\left(\pi x^m\right)\right)^t,\ 0 \le x \le 1 \tag{8}$$

In Equation (8), the parameter m which is defined by Equation (9), is used to create asymmetric bumps. Here, C_B/l_B represents the degree of asymmetry and is in the range of (0,1). $C_B/l_B = 0.5$ represents a symmetric bump.

$$m = \frac{\ln(0.5)}{\ln(c_B/l_B)} \tag{9}$$

The ranges of variation for the bump geometry parameters are given below (all the variables are non-dimensionalised with the airfoil chord length).

$$\begin{cases} 0 \le h_B \le 0.01c \\ 0.1 \le x_0/l_B \le 0.55 \\ 0.4 \le c_B/l_B \le 0.85 \\ 0.5 \le t \le 2 \\ 0.15 \le l_B \le 0.3 \end{cases} \tag{10}$$

Limits of different design variables are selected by considering various references such as (Sommerer et al., 2000; Tian et al., 2011). In order to reach a more realistic design in the optimisation process, 15% of the airfoil's cord adjacent to the trailing edge is devoted to the flap and the bump is considered ahead of this region.

6. Optimisation results for the 2D bump in constant-lift condition

We will first optimise the performance of the root section of the ONERA-M6 wing using an appropriate SCB. Later we will use this information for comparison of 2D and 3D SCBs. There are two different optimisation strategies with different motivations. One is optimisation under constant angle of attack, as followed in Koenig et al. (2007). The motivation here is to increase the payload of an existing aircraft without a major change in the wing installation angles. In this strategy as explained in Koenig et al. (2007) after optimisation the total angle of attack is changed in flight if the previous lift coefficient is required. The other strategy is optimisation under constant *Cl* constraint (variable angle of attack), which is followed here. To achieve this, the algorithm developed by the authors (Mazaheri & Nejati, 2016) is used which continuously changes the angle of attack (AOA) during the optimisation process. The cost function for this constrained optimisation problem is the drag coefficient. The optimisation procedure is applied to optimise five design parameters of an SCB for the ONERA-M6 airfoil for the flight condition stated in Table 2, and results are shown in Tables 3 and 4. One observes that the optimisation process decreases the drag coefficient and improves

Table 3. The 2D bump optimisation results for the ONERA-M6 root section in constant *Cl* condition.

Design parameter	x_0/c	c_B/c	t	l_B/c	h_B/c
Initial value	0.500	0.500	1.00	0.200	0.00
Final value	0.512	0.542	0.936	0.299	0.00854

Table 4. Results of the 2D optimised bump for the ONERA-M6 root section.

Flight condition	M	α	Cl	Cd_t	L/D	$-\%\Delta Cd$	$\%\Delta L/D$
Initial value	0.839	3.06	0.331	0.0429	7.71	0.0	0.0
Final value	0.839	2.58	0.331	0.0353	9.40	16.5	21.9

the aerodynamic efficiency of the bumped airfoil by about 16 and 22 per cent in comparison with the original airfoil, respectively.

For better understanding of the physics of bump compressibility effects and comparison of the flow field in different designs, the ONERA-M6 airfoil pressure coefficient for two different cases are compared: the original un-bumped airfoil and the airfoil with the optimised bump. Results are shown in Figure 5. The pressure distribution around the shock wave on the suction side of the original clean airfoil has three main components:

- Initial expansion waves (called **E**) upstream the normal shock wave,
- A non-isentropic strong compressive shock wave (called **NC**),
- Isentropic compression waves downstream the shock wave (called **IC**).

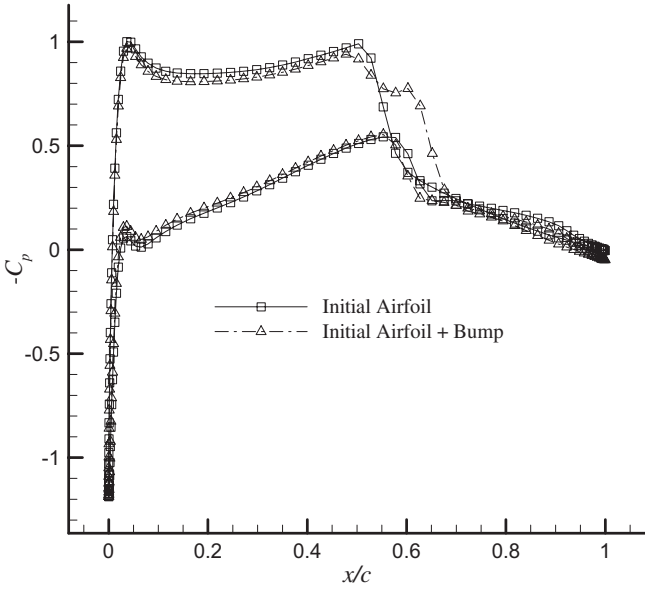

Figure 5. The pressure coefficient distribution around the ONERA-M6 airfoil (M_∞ = 0.839, Cl = 0.331).

This **E**-**NC**-IC structure is changed to a five wave model i.e. **E**-**IC**-**E**-**NC**-**IC** using the optimised bump. The **IC** generated after the initial **E** waves, does not allow very low pressures to occur over the airfoil, which may trigger a very strong shock wave. A very similar detailed physical discussion is presented in (Mazaheri, Nejati, & Kiani, 2016) for two other transonic airfoils.

Figure 6 shows the pressure contours with flow stream-lines for the above two cases. The wave structure over the original airfoil (Figure 6(a)) consists of the expansion waves, a strong shock wave and compression waves, but for the bumped case (Figure 6(b)), the flow pattern over the airfoil is initiated with the expansion waves, and then the compression waves are formed over the uphill side of the bump. Then, after the crest point a weak expansion occurs, and then a weakened shock wave happens and is finally followed by compression waves.

The optimisation process is a delicate match and balance among these five components of the compressible flow, of course, including their interaction with the boundary layer, and the flow separation downstream of the shock wave. Figure 7 shows the skin friction coefficient around the airfoil, and shows that the shock control bump decreases the boundary layer thickness in the region of the shock wave, and decreases the separated flow region after the shock wave. The shock wave is moved towards the trailing edge. Interaction of the shock wave with the compression waves generated by the bump has resulted in a less entropy generating shock wave, and the separated flow region is shrunk and is moved backward. This figure also displays an increase in viscous drag which is of course smaller than the decrease in wave drag.

7. Modelling of the 3D bump geometry on ONERA-M6 wing

Here, we introduce two different geometrical models to generate a three-dimensional bump over a finite span wing. The first model is called linear and the second is called periodic.

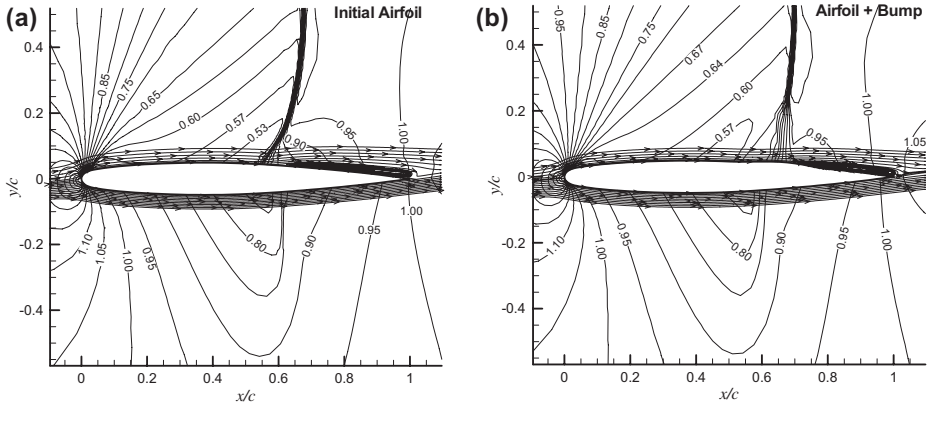

Figure 6. The pressure contours with flow stream-lines for the ONERA-M6 airfoil, (a) without the bump and (b) with the optimised bump ($M_\infty = 0.839$, $Cl = 0.331$).

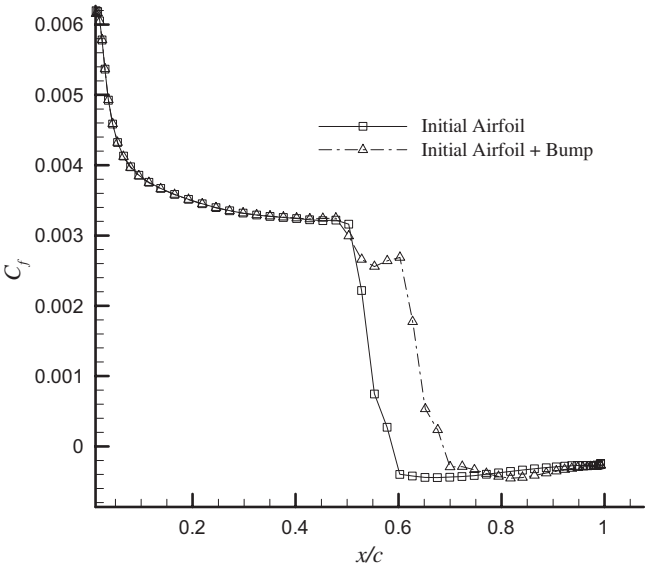

Figure 7. Comparison of the friction coefficient distribution over root section of ONERA-M6 wing, $M_\infty = 0.839$, $Cl = 0.331$.

- *Linear model*

We consider a two-dimensional SCB with five parameters at the root section of the wing, and another one at the tip section, as described in Section 5. In this model, all bump parameters vary linearly between the tip and the root sections of the wing. For example, the maximum value for the height of the bump varies as:

$$h_B(z) = h_{B,root} - \left(h_{B,root} - h_{B,tip}\right) \times z/b \tag{11}$$

The root is located at $z/b = 0$, therefore the maximum height is located at the root section, and linearly varies till the tip section. b is the wing semi-span and equals 1.487 here. Therefore, we have 10 design variables for the 3D SCB with a linear variation model.

- *Periodic model*

In this model, we have divided the wing semi-span to six equal segments, i.e. seven sections. At each section we consider a 2D SCB with five parameters. Each parameter in each segment is varied by a squared sine function, given below. For example, the height of the SCB during the first two segments between sections $z/b = 0$ and $z/b = 2s_c = 0.3334$ is varied by the following function:

$$\begin{cases} h_B^1(z) = h_{SCB1} - \left(h_{SCB1} - h_{SCB1}\right)\left(1 - \sin^2\left(\dfrac{\pi}{2}\left(1 - \dfrac{z/b}{s_C}\right)\right)\right) & if \quad 0 \le z/b \le s_C \\ h_B^2(z) = h_{SCB2} - \left(h_{SCB2} - h_{SCB3}\right)\left(1 - \sin^2\left(\dfrac{\pi}{2}\left(1 - \dfrac{z/b - s_C}{s_C}\right)\right)\right) & if \quad s_C \le z/b \le 2s_C \end{cases} \tag{12}$$

Here $h_B{}^1$ represents the SCB maximum height between the first and second stations. h_{SCB1} is the maximum height of the bump at the first station, i.e. $z/b = 0$. Since we have seven sections, the total number of design parameters is 35 for the 3D SCB with a periodic variation model. These parameters are sought through the optimisation procedure. Since the periodic model includes 35 parameters, one expects that these SCBs shall be more effective in drag reduction or performance improvement.

8. Results of optimisation of the 3D bump on ONERA-M6 wing

Here, we use the above models to improve performance of an ONERA-M6 wing in the same flight condition given in Table 2. With a constant lift constraint, the design variables are optimised to have the minimum drag coefficient or maximum aerodynamic efficiency, therefore the angle of attack varies during the optimisation process.

For the linear model, we have 10 design parameters, which are initially assumed to be equal to the optimised similar 2D case at both root and tip sections. The final optimised values of design variables at both root and tip sections are given in Table 5. Similarly Table 6 shows the results for the periodic variation model, i.e. all 35 design variables, five for each section. We have seven sections starting from the root section, and ending in the tip section.

In fact, the algorithm presented here uses a sensitivity analysis in each iteration to find those design variables which are more effective to minimise the cost function. Gradients of the cost function, i.e. the drag coefficient, respect to all design variables for both linear and periodic SCBs are given in Tables 7 and 8. Based on values of sensitivity derivatives at one of initial iterations one observes

Table 5. The optimisation results for the linear model bump.

Design parameter	x_0/c	c_B/c	t	l_B/c	h_B/c	z/b
SCB_{root}	0.581	0.618	1.13	0.263	0.00432	
						$0.000 < z/b < 1.000$
SCB_{tip}	0.131	0.602	0.936	0.299	0.00754	

Table 6. The optimisation results for the periodic model bump.

Design parameter	x_0/c	c_B/c	t	l_B/c	h_B/c	z/b
SCB_1	0.562	0.598	1.21	0.257	0.00378	
						$0.000 < z/b < 0.167$
SCB_2	0.517	0.605	1.03	0.249	0.00621	
						$0.167 < z/b < 0.333$
SCB_3	0.437	0.611	0.982	0.268	0.00485	
						$0.333 < z/b < 0.500$
SCB_4	0.351	0.586	1.26	0.271	0.00742	
						$0.500 < z/b < 0.667$
SCB_5	0.281	0.595	1.06	0.281	0.00511	
						$0.667 < z/b < 0.834$
SCB_6	0.198	0.602	1.17	0.283	0.00861	
						$0.834 < z/b < 1.000$
SCB_7	0.141	0.587	1. 09	0.286	0.00631	

Table 7. Sensitivity of the cost function respect to all design variables, linear bump.

Sensitivity respect to design variables	df/dx_0	df/dc_B	df/dt	df/dl_B	df/dh_B	z/b
SCB_{root}	1.333	−8.321	−0.235	−5.326	−13.235	
						$0.000 < z/b < 1.000$
SCB_{tip}	−1.678	10.061	0.325	6.352	−28.325	

Table 8. Sensitivity of the cost function respect to all design variables, periodic bump.

Sensitivity respect to design variables	df/dx_0	df/dc_B	df/dt	df/dl_B	df/dh_B	z/b
SCB_1	−2.651	−7.422	−0.135	−4.652	−10.321	
						$0.000 < z/b < 0.167$
SCB_2	−1.112	−7.982	0.523	−5.236	−12.701	
						$0.167 < z/b < 0.333$
SCB_3	2.924	6.235	0.182	5.032	−10.863	
						$0.333 < z/b < 0.500$
SCB_4	−2.099	9.055	0.325	−7.023	−17.333	
						$0.500 < z/b < 0.667$
SCB_5	−1.877	−8.665	−0.208	−6.422	−15.308	
						$0.500 < z/b < 0.667$
SCB_6	−1.923	11.413	0.332	7.002	−20.111	
						$0.834 < z/b < 1.000$
SCB_7	1.665	−9.552	−0.301	6.923	−23.077	

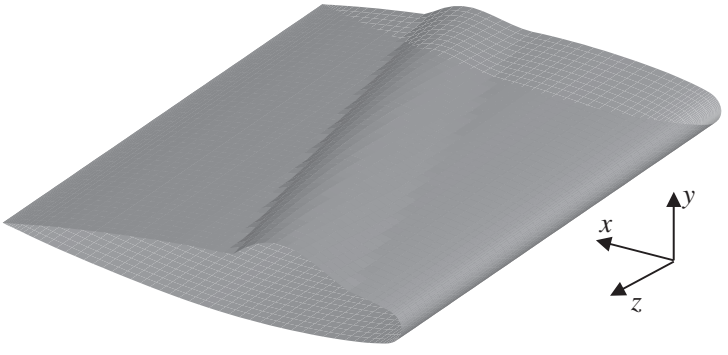

Figure 8. The linearly varying SCB geometry over an ONERA-M6 wing (SCB height scaled up).

that the bump height and stream-wise location of the crest point are the most important parameters.

Figures 8 and 9 show the generated 3D bumps over the wing. The maximum height of the linear model varies linearly from root to tip, and its non-dimensional value increases from 0.00432 to 00754. For the periodic model, according to Table 6 the non-dimensional maximum height alternatively varies along the span. Figure 10 shows the convergence history for the first model. In each optimisation cycle the flow equations and the adjoint equations are solved once, which takes about 16 h. This figure shows that the drag coefficient non-dimensionalised with its initial value, decreases very uniformly during the optimisation process.

Table 9 compares the aerodynamic performance of the original wing with both optimised wings. One observes that the linear model improves the performance

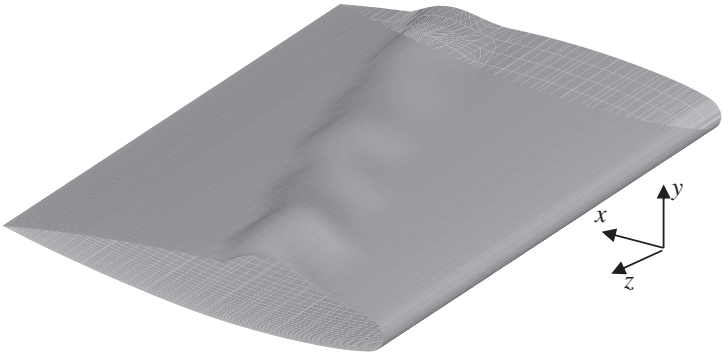

Figure 9. The periodic varying SCB geometry over an ONERA-M6 wing (SCB height scaled up).

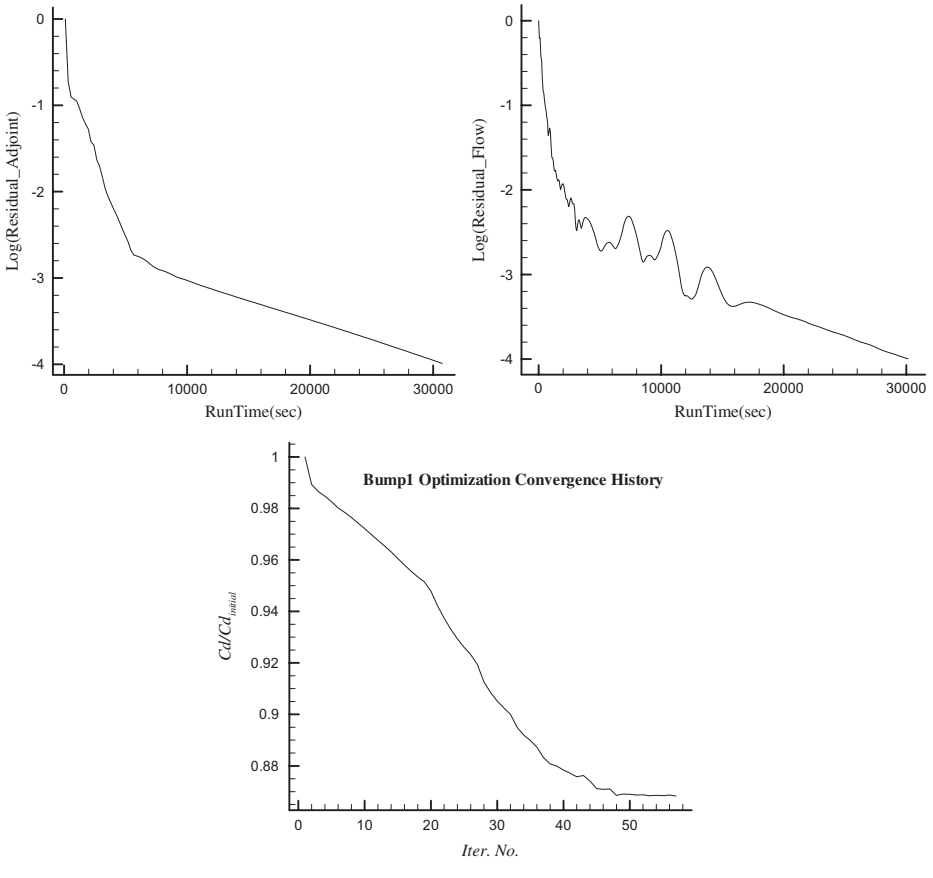

Figure 10. The optimisation convergence history for using the linearly varying SCB on an ONERA-M6 wing.

about 10.3% while the periodic model has a 17.8% improvement. One may compare Tables 4 and 9 to find overall performance difference of two- and three-dimensional SCBs. Although the two-dimensional SCB is more effective (i.e. the

Table 9. The aerodynamic coefficients and improvements for the original and two bumped ONERA-M6 wings at $M_\infty = 0.8395$.

ONERA-M6 wing	*CD*	*CL*	*L/D*	$-\%\Delta CD$	$\%\Delta L/D$
Without bump	0.0179	0.262	14.6	0.0	0.0
With linear bump	0.0163	0.263	16.1	8.94	10.3
With periodic bump	0.0152	0.262	17.2	15.1	17.8

non-dimensional aerodynamic efficiency is increased more than 21%), the real 3D configuration is still very effective and promising (more than 17% for the periodic model). Also, one may note that more complex geometrical models may push this numbers to higher values.

In a 3D flow, a periodic SCB structure works better than a linear configuration. This idea is observed by many people. The flow across a periodic SCB is inherently three-dimensional, and this gives rise to additional effects that do not occur in the case of two-dimensional bumps (and also linear 3D bump). One major effect is the span-wise influence of the bump-induced compression-waves, well beyond its actual span.

The main difference of a 2D (or linear 3D) and a 3D periodic SCB is probably the 3D structure of the boundary layer over the SCB. This includes generation of two pairs of anti-rotating vortices as studied by Colliss et al. (2014). This is easily detected by measuring the pressure gradient in the span-wise direction. Many inter-phenomena interactions are present here between the 3D structure of the boundary layer, shock wave configuration, and expansive and compressive inviscid waves generated by the SCB. The anti-rotating vortices induce a downwash over the SCB surface and the wake region after it. They energise the boundary layer, therefore prevent or delay the flow separation at the higher angle of attack or on the flap and help to decrease the pressure drag. In fact, in this situation the periodic SCB acts like a vortex generator. The relative strength of these two pairs of vortices significantly affect their interaction with the boundary layer. In fact, the advantage of our algorithm is that considers all these complex interactions to minimise the cost function based on our desired performance criteria.

Another effect which is most significant in the 3D periodic bump is that because the bump shape changes along the span-wise direction the flow accelerates along this direction and this phenomenon affects the separation region due to abrupt flow change induced after the bump crest point and consequently the boundary layer thickness and the separation zone are decreased in this area. Figures 14 and 17 show this fact.

Figure 11 compares the pressure distribution over four sections of these three wings, i.e. the original wing and both optimised wings. There are two common observations in all these four figures. First observe that at all sections the SCB has changed the compressible flow structure from a three-wave pattern to a five-wave pattern, as described in our analysis for the two-dimensional bump in Section 7. The original shape has a three-wave E-NC-IC structure, while the optimised wing

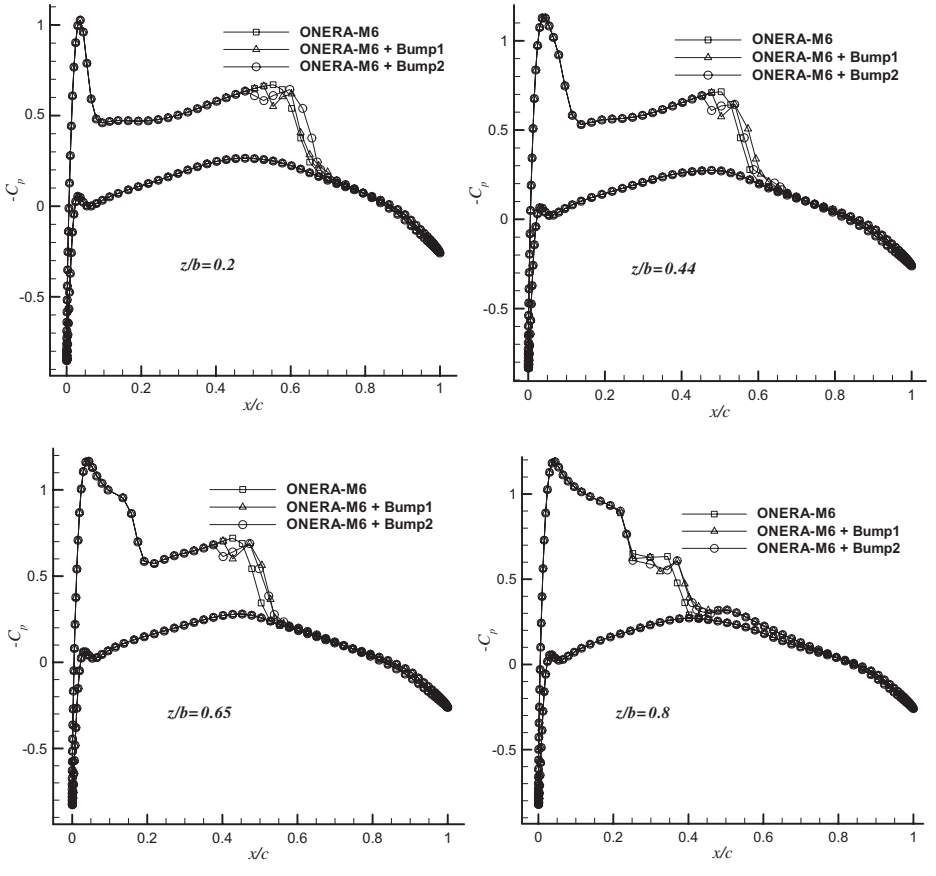

Figure 11. The pressure coefficient distribution over the wing surface for the original and two bumped ONERA-M6 wings at four span-wise stations.

has a five-wave structure (E-IC-E-NC-IC) in all span-wise sections. Both linear and periodic bumps have moved the shock a little towards the trailing edge. As expected the pressure distribution over the pressure side is almost similar for all configurations. The pressure contours at $z/b = 0.65$ for these three wings are shown in Figure 12.

Figure 13 shows distribution of the surface friction coefficient at station $z/b = 0.6$. The SCB has decreased the boundary layer thickness and the separation zone in both bumped wing, but the height of the bump has increased the boundary layer thickness near the trailing edge. The more energetic boundary layer profile after the separation zone increases the contribution of viscous friction in the total drag. The main shock wave is delayed a little bit in both cases.

One important issue in application of an SCB is its sensitivity to variation in the flight conditions. While complete analysis of this issue needs to much more computations, an initial study is accomplished here to show how the aerodynamic performance of the SCB is deteriorated by a perturbation in the flight

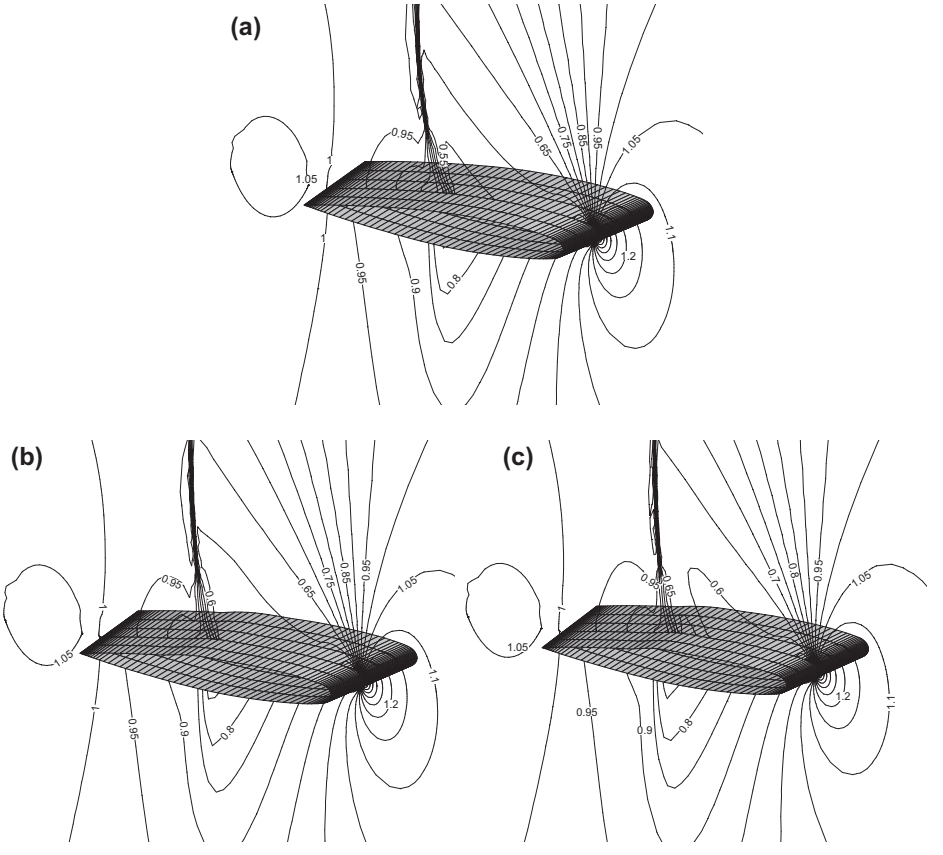

Figure 12. The pressure contours for the ONERA = M6 wing at $z/b = 0.65$, a) without bump, b) the linear model bump, c) the periodic bump.

Mach number. For this study, we have simulated the flow over the ONEA-M6 wings for two adjacent Mach numbers. i.e. $M = 0.83$ and $M = 0.85$ (The original Mach number is 0.8395). To make the comparison fairer, we change the angle of attack in each case to have the lift constraint satisfied. Tables 10 and 11 show the aerodynamic performance at these flight conditions. One observes that the same optimised SCB configuration improves the aerodynamic performance at both new flight conditions, while the improvements are higher for linear configuration at the higher Mach number of 0.85, but the periodic configuration behaves fairly similar for both Mach numbers. The aerodynamic efficiency for linear and periodic geometrical models are, respectively, 5.92 and 8.28% for $M = 0.83$, 10.3 and 17.8% for $M = 0.8395$, and 6.31 and 8.12% for $M = 0.85$.

One observes that the design is fairly sensitive to the Mach number change, and the off-design performance is deteriorated far from the design point. To decrease sensitivity of the optimal shape to off-design conditions, one need to use multi-point or robust optimisation techniques to find a solution which has a lower performance at any single point, but possesses an overall higher

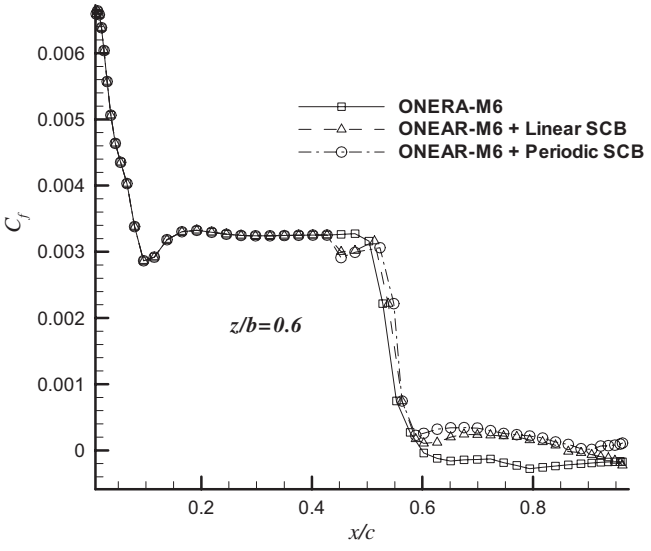

Figure 13. The friction coefficient distribution for the original and two bumped ONERA-M6 wings at section $z/b = 0.6$.

Table 10. The aerodynamic coefficients and improvements for the original and two bumped ONERA-M6 wings at $M_\infty = 0.83$.

ONERA-M6 wing	*CD*	*CL*	*L/D*	−%Δ*CD*	%Δ*L/D*
Without bump	0.0171	0.290	16.9	0.0	0.0
With linear bump	0.0162	0.291	17.9	5.26	5.92
With periodic bump	0.0159	0.291	18.3	7.02	8.28

Table 11. The aerodynamic coefficients and improvements for the original and two bumped ONERA-M6 wings at $M_\infty = 0.85$.

ONERA-M6 wing	*CD*	*CL*	*L/D*	−%Δ*CD*	%Δ*L/D*
Without bump	0.0182	0.201	11.1	0.0	0.0
With linear bump	0.0170	0.200	11.8	6.59	6.31
With periodic bump	0.0168	0.202	12.0	7.69	8.12

performance over a predefined range of conditions. Authors have implemented this idea for 2D SCBs and 3D ones on an un-swept wing (Mazaheri, Nejati, & Kiani, 2016; Mazaheri, Nejati, Kiani, & Taheri, 2016), and they would apply this to a swept wing 3D configuration in the near future.

Figure 14 shows the streamlines in the vicinity of the wing surface between the root section ($z/b = 0.0$) and $z/b = 0.333$ section. Without an SCB at the base Mach number, there is a strong interaction between the three-dimensional shock wave and the boundary layer, which results in a huge separation region after the shock wave, and extended to the trailing edge. Both linear and periodic SCB models decrease the size of this separated region, while the periodic model is much more effective in reducing this region. This could partly

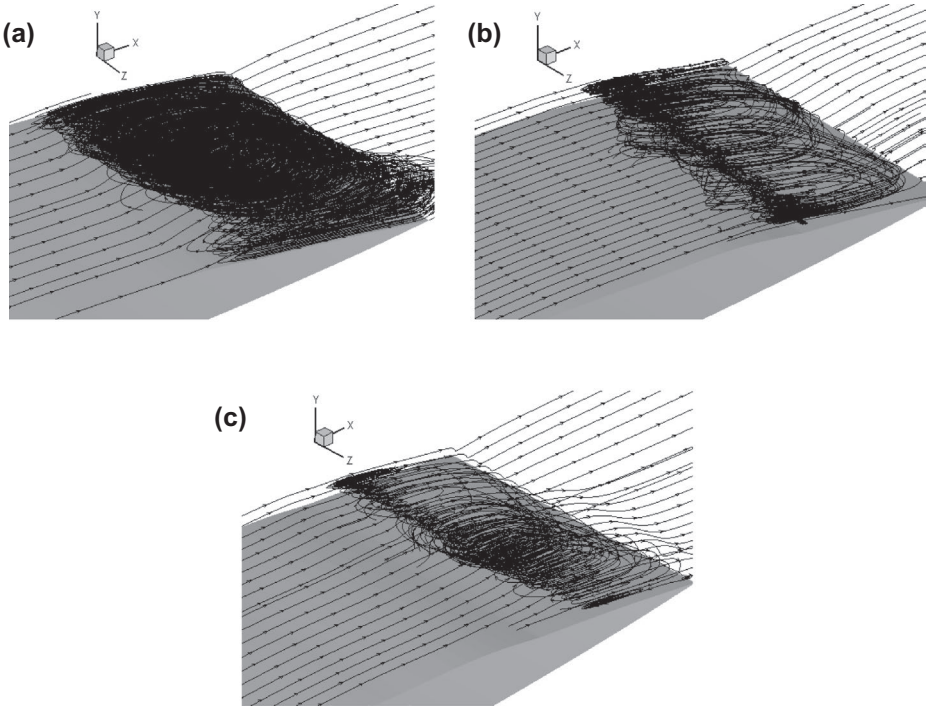

Figure 14. The flow stream-lines for the ONERA = M6 wing at $0.0 < z/b < 0.33$, (a) without bump, (b) the linear model bump, and (c) the periodic bump.

explain why the periodic model produces a better aerodynamic performance. One shall note that the overall phenomenon needs to more consideration, since it is shown that a periodic variation in geometrical parameters make the flow structure more favourable respect to a uniformly varying geometry.

The non-uniform bumps in the span-wise direction, induce higher velocities close to the bump crest, and this will energise the boundary layer, and locally decreases the boundary layer thickness. One reason for this performance improvement could be that the span-wise variation in the average velocity close to the wing surface acts like a span-wise shear layer, which induces vortices normal to the wing surface and this, produces a very strong inductive source for flow attachment. In fact structure of these vortices is optimised during optimisation procedure to result in a final favourable flow field. One concludes that a discrete 3D bump combines the shock wave weakening property of a 2D bump with the vortex generating capability, which suppresses the stream-wise separation at the rear part of the bump at off-design conditions and also reduces the potential trailing edge separation.

Figure 15 simultaneously compares the shock structure for the original wing and the SCB with linear geometrical variation at three span-wise sections. This clearly shows that the new five-wave pattern pushes the shock wave towards the

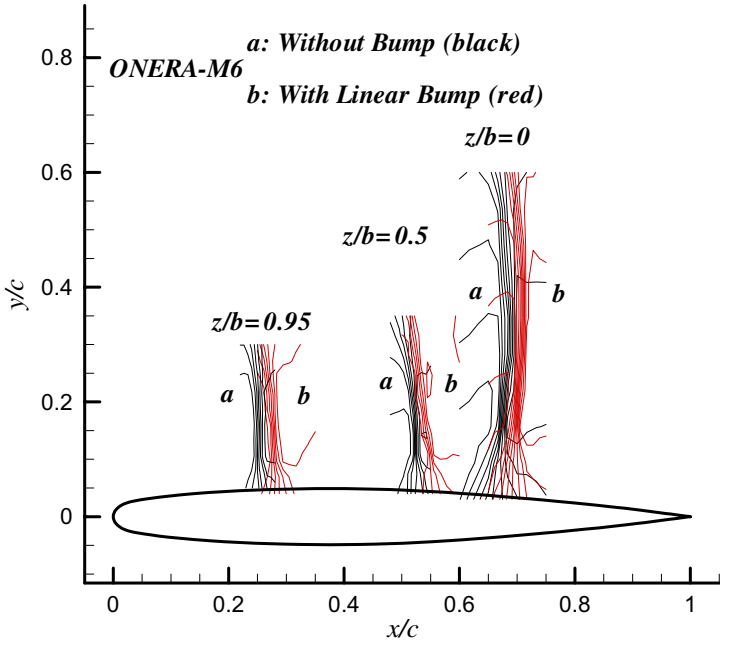

Figure 15. The shock wave locations for the ONERA-M6 wing at different stations for the clean wing and linear bump.

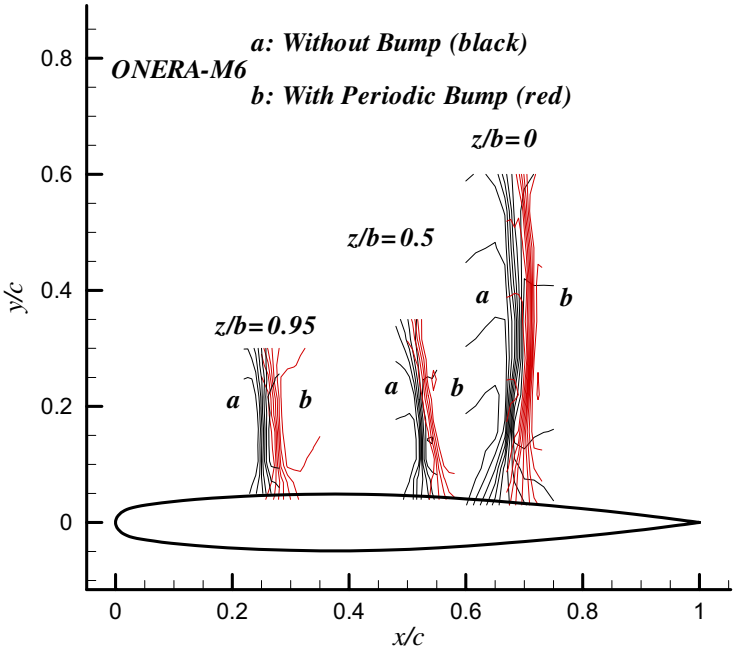

Figure 16. The shock wave locations for the ONERA-M6 wing at different stations for the clean wing and periodic bump.

trailing edge. Figure 16 shows similar comparisons for the original and the periodically varying geometrical model.

At high Mach numbers, the shock wave and its interaction with the boundary layer is very strong. Therefore it is very important to study these interactions to achieve an optimised configuration. Figure 17 shows the boundary-layer profile for the ONERA-M6 at z/b = 0.5 for different locations (from 70% up to 85% of the chord) and compares the wing with the two model SCBs with the case of the wing without SCB. The linear SCB and the periodic SCB have reduced the boundary-layer thickness after the shock position with respect to the clean ONERA-M6 wing. This figure also shows that, the periodic SCB is more effective than the linear one in reducing the boundary layer thickness. In fact the periodic bump combines the shock wave weakening property of the linear bump with the vortex generating capability, which suppresses the stream-wise separation at the rear part of the bump at off-design conditions and also reduces the potential trailing edge separation. In other words, the advantage of periodic bumps lies in the production of stream-wise vortices.

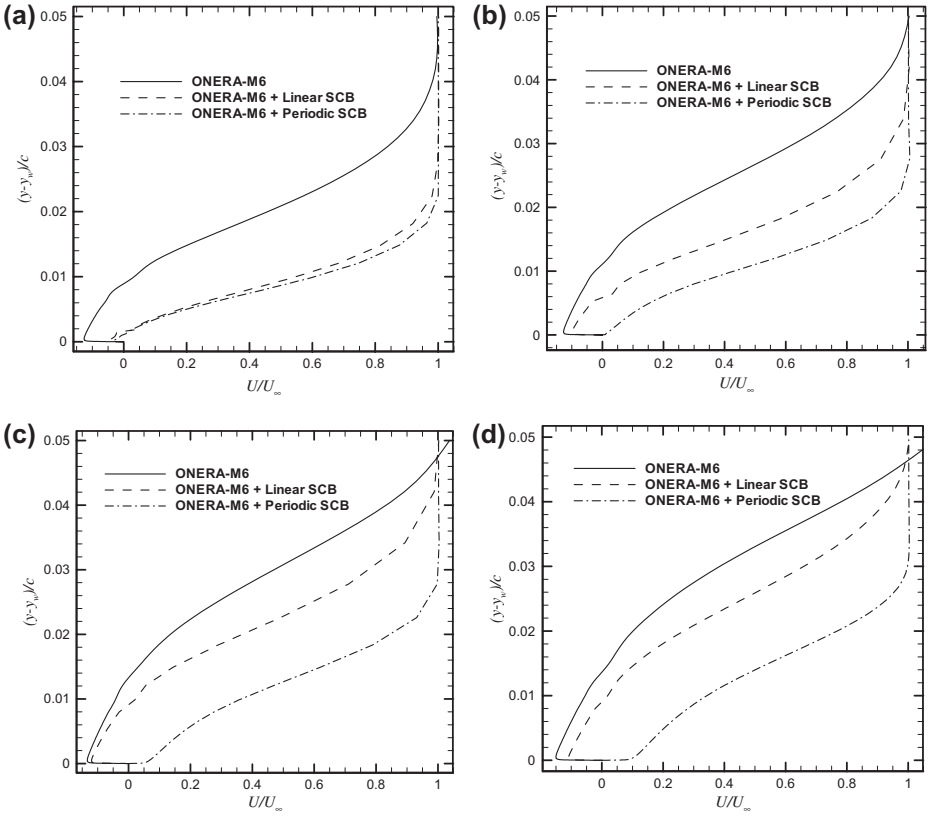

Figure 17. Boundary-layer velocity profiles for the ONERA-M6 wing at $z/b = 0.5$ with and without the optimised SCBs, at different stations: (a) x/c = 0.70, (b) x/c = 0.75, (c) x/c = 0.80, and (d) $x/c = 0.85$.

9. Conclusions

It was shown that the SCB may improve the aerodynamic performance and reduce the drag of transonic wings at high speed flight conditions. Extension of the SCB concept to real three-dimensional wing configurations is studied here. Many interesting physical observations are given which help in a better understanding of how the bump may change the flow structure in benefit of a better aerodynamic efficiency.

Two new three-dimensional models for geometrical modelling of bumps over a swept ONERA-M6 wing are introduced and studied. The 3D SCBs are optimised using an adjoint gradient-based scheme, and results are compared with the two-dimensional case. It is shown that in the 3D case the overall performance improvement and the boundary-layer structure, and also the compressible wave patterns are very much similar to the two-dimensional case. Both 2D and 3D bumps have changed the far-field (i.e. out of the boundary layer) **E**-**NC**-**IC** wave structure to a more appropriate **E**-**IC**-**E**-**NC**-**IC** wave pattern.

The new wave structure weakens the shock wave close to the surface, therefore thickness of the boundary layer close to the surface in the shock wave region decreases, resulting in a more energetic boundary layer and the separation is delayed. Moreover, we have observed some three-dimensional phenomena resulting from generation of a span-wise shear layer which is matched for a more favourable flow structure. This phenomena needs to further studies with higher computational resources to be completely understood.

List of symbols

$\mathbf{A}^T$	Jacobian of convective flux
$\mathbf{b}$	Design parameter vector
c	Speed of sound
C	Airfoil cord line
C_B/l_B	Bump degree of symmetry
Cd_p	Pressure drag coefficient
Cd_t	Airfoil drag coefficient
Cd_v	Viscous drag coefficient
C_f	Skin friction coefficient
Cl	Airfoil lift coefficient
C_p	Pressure coefficient
C_w	Relaxation parameter
ds	Surface element
f	Hicks-Henne Sine-function
F	Cost function for the constrained optimisation problem
f_j	Deterministic component

$\mathbf{f}^{inv}$	Inviscid flux vector
$\mathbf{f}^{vis}$	Viscous flux vector
$\mathbf{G}$	Gradient vector of cost function
g	Optimisation constraint
h_B	Maximum bump height
k	Turbulent kinetic energy
l_B	Bump length
L/D	Aerodynamic efficiency
$\mathbf{M}^{-T}$	Transition matrix of non-conservative variables
M_∞	Free stream Mach number
n_x, n_y	Component of the unit normal vector
p	Static pressure
p_{tar}	Static pressure target on airfoil surface
P_∞	Free stream pressure
q_k	Heat flux
r	Penalty function parameter
Re_∞	Free stream Reynolds number
$\mathbf{S}i$	Search direction vector in iteration No
S_w	Airfoil surface
t	Bump slope parameter
T	Static temperature
$\mathbf{U}$	Vector of flow variable
u,v,w	Cartesian velocity component
V	Contra variant velocity
V_∞	Magnitude of free stream velocity
x,y,z	Cartesian coordinate system
x_0	Bump starting point
Y^+	Non-dimensional wall coordinate
α	angle of attack, deg
γ	Ratio of specific heat coefficient at constant pressure &volume
δ_{km}	Kronecker symbol
κ	Thermal diffusivity coefficient
λ	Second viscosity coefficient
λ^*	Optimum step length
μ	Dynamic viscosity coefficient
μ_∞	Free stream viscosity coefficient
τ_{km}	Component of viscous stress tensor
ρ	Density
ρ_∞	Free stream density
ω	Turbulent specific dissipation rate
$\boldsymbol{\psi}$	Vector of adjoint variable
$\boldsymbol{\Phi}$	Cost function for the unconstrained optimisation problem

Acknowledgement

The authors acknowledge that there is no funding source for this study.

Disclosure statement

No potential conflict of interest was reported by the authors.

References

Abdellah, H. (2012). Large-eddy simulation of shock-boundary-layer interaction. *AIAA Journal, 50*(12), 2919–2927.

Abdul Hamid, M. D., Toufique Hasan, A. B. M., Alimuzzaman, S. M., Matsuo, S., & Setoguchi, T. (2014). Compressible flow characteristics around a biconvex arc airfoil in a channel. *Propulsion and Power Research, 3*(1), 29–40.

Anderson, W. K., & Venkatakrishnan, V. (1997). Aerodynamic design optimization on unstructured grids with a continuous adjoint formulation. *Elsevier, Journal of omputational & Fluids*, *28*, 443–480. https://doi.org/10.1016/S0045-7930(98)00041-3 (1999) AIAA-97-0643.

Ashill, P. R., Fulker, J. L., & Shires, A. (1992, March). *A novel technique for controlling shock strength of laminar-flow aerofoil sections*. Paper presented in the First European Forum on Laminar Flow Technology, Hamburg.

Bhattacharjee, S., Ahsan, M., & Mohammad, M. (2007). Numerical analysis of shock and boundary layer control over NACA0012 by contour bump, surface cooling and heating. In *Proceedings of the International Conference on Mechanical Engineering* (pp. 29–31), Dhaka.

Blazek, J. (2005). *Computational fluid dynamics: Principles and applications* (2nd ed.). Amsterdam: Elsevier.

Bruce, P. J. K., & Babinsky, H. (2012). Experimental study into the flow physics of three-dimensional shock control bumps. *Journal of Aircraft, 49*(5), 1222–1233.

Colliss, S. P., Babinsky, H., Nubler, K., & Lutz, T. (2014). Joint experimental and numerical approach to three dimensional shock control bump research. *AIAA Journal, 52*(2), 436–446

Eastwood, J. P., & Jarrett, J. P. (2012). Toward designing with three-dimensional bumps for lift/drag improvement and buffet alleviation. *AIAA Journal, 50*(12), 2882–2898.

Evans, M. R., Hynes, R. J., Norman, D. C., & Thomasson, R. E. (1984). Automatic flight control modes for the AFTI/F-111 mission adaptive wing aircraft. *AGARD-CP-384, 25*.

Giles, M. B., & Pierce, N. A. (1997). *Adjoint equations in CFD: Duality, boundary conditions and solution behavior*, Snowmass Village, CO, USA. https://doi.org/10.2514/6.1997-1850. AIAA-97-1850.

Koenig, B., Paetzold, M., Lutz, T., & Kraemer, E. (2007). Shock control bumps on flexible and trimmed transport aircraft in transonic flow. In *New Results in Numerical and Experimental Fluid Mechanics* (Vol. 96, pp. 80–87), Berlin.

Lee, D. S., Bugeda, G., Periaux, J., & Onete, E. (2010). *Active flow control bump design using hybrid Nash-game coupled to evolutionary algorithms*. V European Conference on Computational Fluid Dynamics ECCOMAS CFD, Lisbon.

Lee, D. S., Bugeda, G., Periaux, J., & Onete, E. (2012). Robust active shock control bump design optimization using hybrid parallel MOGA. *Journal of Computational & Fluids, 80*, 214–224.

Mayer, R., Lutz, T., & Kraemer, E. (2015). *Toward numerical optimization of buffet alleviating three-dimensional shock control bumps*. 6th European Conference for Aerospace Sciences.

Mazaheri, K., Kiani, K. C., Nejati, A., Zeinalpour, M., & Taheri, R. (2015). Optimization and analysis of shock wave/boundary layer interaction for drag reduction by shock control bump. *Journal of Aerospace Science and Technology, 42*, 196–208. doi:10.1016/j.ast.2015.01.007

Mazaheri, K., & Nejati, A. (2016). The multi-point optimization of shock control bump with constant-lift constraint enhanced with suction and blowing for a supercritical airfoil. *Flow, Turbulence and Combustion, 96*(3), 639–666. doi:10.1007/s10494-015-9671-8

Mazaheri, K., Nejati, A., & Kiani, K. C. (2016). Application of the adjoint multi-point and the robust optimization of shock control bump for transonic aerofoils and wings. *Engineering Optimization, 48*(11), 1887–1909. doi:10.1080/0305215X.2016.1139811

Mazaheri, K., Nejati, A., Kiani, K. C., & Taheri, R. (2016). The application of the gradient-based adjoint multi-point optimization of single and double shock control bumps for transonic airfoils. *Shock Waves, 26*(4), 491–511. doi:10.1007/s00193-015-0591-2

Milholen, II, W. E., & Lewis, L. R. (2005). *On the application of contour bumps for transonic drag reduction*. AIAA 43rd Aerospace Sciences Meeting and Exhibit, AIAA-2005-0462, Reno.

Nadarajah, S., & Jameson, A. (2000). *A comparison of the continuous and discrete adjoint approach to automatic aerodynamic optimization*. AIAA 38th Aerospace Sciences Meeting and Exhibit, AIAA-2000-0667, Reno.

Nejati, A., & Mazaheri, K. (2016). Drag reduction by a multi-point optimised hybrid flow control method for two supercritical airfoils. *European Journal of Computational Mechanics, 25*(5), 359–387. doi:10.1080/17797179.2016.1240535

Ogawa, H., Babinsky, H., Pätzold, M., & Lutz, T. (2008). Shock-wave/boundary-layer interaction control using three-dimensional bumps for transonic wings. *AIAA Journal, 46*(6), 1442–1452.

Patzold, M., Lutz, T. H., Kramer, E., & Wagner, S. (2006). Numerical optimization of finite shock control bumps. In *AIAA 44th Aerospace Sciences Meeting and Exhibit* (pp. 9–12). Reno.

Qin, N., Wong, W. S., & Le Moigne, A. (2008). Three-dimensional contour bumps for transonic wing drag reduction. *Journal of Aerospace Engineering, 222*(5), 619–629.

Qin, N., Zhu, Y., & Shaw, T. H. (2004). Numerical study of active shock control for transonic aerodynamics. *International Journal of Numerical Methods for Heat & Fluid Flow, 14*(4), 444–466.

Ramezani, A., & Mazaheri, K. (2009). Multi-grid convergence acceleration for implicit and explicit solution of Euler equations on unstructured grids. *International Journal for Numerical Methods in Fluids, inter science Wiley publication, 62*(9), 994–1012.

Rao, S. S. (1996). *Engineering optimization: Theory and practice* (3rd ed.). New York, NY: Wiley.

Schmitt, V., & Charpin, F. (1979). *Pressure distributions on the ONERA-M6-wing at transonic mach numbers, experimental data base for computer program assessment*. Report of the Fluid Dynamics Panel Working Group 04, AGARD AR 138.

Snyman, J. A. (2005). *Practical mathematical optimization, an introduction to basic optimization theory and classical and new gradient based algorithms*. New York, NY: Springer. ISBN 0-387-24348-8.

Sommerer, A., Lutz, T., & Wagner, S. (2000). *Numerical optimization of adaptive transonic airfoils with variable camber*. 22nd Congress of International Council of the Aeronautical Sciences, Paper ICAS 2000-2.11.1, Harrogate.

Stanewsky, E., Delery, J., Fulker, J., & de Matteis, P. (Eds.) (2002). Drag reduction by shock and boundary layer control. *Notes on Numerical Fluid Mechanics and Multi-disciplinary Design, 80*, 3–4.

Tian, Y., Liu, P., & Feng, P. (2011). Shock control bump parametric research on supercritical airfoil. *Science China Technological Sciences, 54*(11), 2935–2944.

Tian, Y., Liu, P., & Li, Z. (2014). Multi-objective optimization of shock control bump on a supercritical wing. *Science China Technological Sciences, 57*(1), 192–202.

Wilcox, D. C. (2006). *Turbulence modeling for CFD* (3rd ed.). La Canada, CA: DCW Industries Inc.

Wong, W. S., Le Moigne, A., & Qin, N. (2007). Parallel adjoint-based optimization of a blended wing body aircraft with shock control bumps. *The Aeronautical Journal, 111*(1117), 165–174.

Yagiz, B., Kandil, O., & Pehlivanoglu, Y. V. (2012). Drag minimization using active and passive flow control techniques. *Aerospace Science and Technology, 17*, 21–31.